Soot and PAH formation in high pressure spray pyrolysis of gasoline and diesel fuels

Kevin Wan*, Julien Manin, Hyung Sub Sim[1]

[a]*Combustion Research Facility, Sandia National Laboratories, 7011 East Ave, Livermore, California, 94550, United States*

Abstract

Time-resolved soot and PAH formation from gasoline and diesel spray pyrolysis are visualized and quantified using diffuse back illumination (DBI) and laser induced fluorescence (LIF) at 355 nm, respectively, in a constant-volume vessel at 60 bar from 1400 to 1700 K for up to 30 ms. The delay, maximum formation rate, and yield of soot and PAHs are compared across fuels and temperatures and correlated with the yield sooting indices on either the mass or mole basis. The delays generally decrease with increasing temperature, and the formation rates of both PAHs and soot generally increase with temperature. The apparent PAH-LIF yield may decrease with temperature due to PAH growth and conversion into larger species, signal trapping, and thermal quneching. Soot yield generally increases with temperature. The mass-based YSI correlates reasonably well with soot delay, but YSI does not correlate well with soot yield. The mass-based YSI is a more appropriate predictor of sooting propensity than the mole-based YSI.

*Corresponding author.
Email address: kwan@sandia.gov (Kevin Wan)
[1]Current address: Department of Aerospace Engineering, Sejong University, Gwangjin-gu, Neungdong-ro, 209, Seoul, Republic of Korea

Keywords: soot, PAH, pyrolysis, diesel, gasoline

1. Introduction

Particulate matter (PM) has a broad impact, with negative effects on human health, the environment, and contributes to global warming. Soot formation has been a longstanding challenge in a wide variety of combustion systems such as light and heavy-duty vehicles, as well as gas turbines and aero-engines. As health and environmental regulations become increasingly strict, the need to understand and predict soot formation in engines and develop strategies to reduce emissions becomes ever higher [1, 2].

Currently, accurate prediction of soot formation in engines using computational fluid dynamics (CFD) is difficult due to the complexity of the problem. The problem begins with the multi-phase liquid spray, requiring accurate predictions of break-up and atomization, as well as the subsequent processes such as evaporation, mixing, ignition and combustion. Real fuels such as gasoline, diesel, and kerosene are composed of hundreds to thousands of different hydrocarbon components, as a result, accurate and efficient modeling of the combustion chemistry is challenging by itself. The most common existing practice is to use a surrogate fuel blend that consists of a few hydrocarbons. This surrogate fuel is built to resemble the behavior of the real fuel and makes modeling the chemistry much more feasible [3]. Finally, understanding the formation of soot particles from gaseous hydrocarbon precursors that condense into solid nanoparticles that grow, and eventually oxidize, presents its own challenge and remains a highly active research area. Each of these phenomena are complicated in their own right, and become much

more so when combined. Thus, there is a need for high-fidelity experimental data on soot formation from fuels at engine relevant conditions.

The key to understanding soot formation lies in understanding polycyclic aromatic hydrocarbon (PAH) chemistry. This has been studied extensively in low-pressure systems such as atmospheric flames [4–6], yet the understanding of PAH chemistry remains incomplete due to the sheer variety of PAHs that can exist. The existing kinetic data for soot formation is currently derived from these low-pressure systems, but it has not been well-studied under high-pressure engine-relevant conditions, where the behavior may change. Studies in both premixed [7, 8] and diffusion [9] flames suggest that soot formation from various small hydrocarbons tends to increase with pressure. On the other hand, shock tube pyrolysis studies generally show less pressure dependence of soot formation of selected fuels [10–12]. In general, the pressure dependence on soot formation can vary widely with different fuels [13–17]. The soot inception mechanism itself remains uncertain: Most currently accepted models rely on PAH dimerization, yet thermodynamics and kinetics indicate that PAH dimerization is unlikely to be a dominant step for soot inception [18, 19], as supported by recent experiments [20]. More recent work has suggested the possibility of resonance-stabilized radicals as a novel pathway to soot formation [21], but this has yet to be implemented in existing kinetic models.

Studying soot formation under pyrolysis conditions is useful because it isolates soot formation from oxygen chemistry. This constrains the modeling problem and provides a more focused guidance for soot model development. In the case of direct-injection gasoline spark-ignition engines, a large por-

tion of soot emissions comes during cold-start, in which liquid fuel is often deposited onto the piston top or cylinder liner as a film [22] and may burn as a pool fire or pyrolyze. Shock tube studies of soot formation via pyrolysis [12, 23, 24] revealed that soot yield exhibits autocatalytic behavior with respect to temperature: Soot yield initially increases with temperature, and then decreases as the temperature increases further, resulting in a bell-shaped curve of the temperature-dependent soot yield. Experimental evidence increasing ambient pressure shifts the bell curve towards lower temperatures and the maximum soot yield tends to increase as well. One limitation with shock-tube studies is that the experimental observation time is limited to a few milliseconds until the expansion wave arrives. Studies on diffusion flames can also serve as a useful reference for pyrolysis. For example, the centerline in the near-burner region of non-lifted coflow diffusion flames is oxygen-deficient and strongly resembles pyrolysis conditions. The soot onset temperature along the centerline of laminar diffusion flames was found to be between 1310 and 1400 K for a variety of small alkane fuels no larger than benzene [25, 26]. In comparison, high pressure fuel pyrolysis of n-dodecane sprays revealed a soot onset temperature around 1450 K [27]. Both differences in diffusion flames versus pyrolysis as well as differences in fuel molecular structure could influence the slightly different observed soot onset temperature.

Metrics are often used to quantify the differences in sooting behaviors of different fuels and a few of them have been called out in fuel specifications. For example, the smoke point, which correlates to soot yield in laminar coflow diffusion flames [28] and fuel molecular structure [29, 30], has been used

as an aviation jet fuel specification [31]. Threshold sooting index (TSI) was introduced to enable predictions of soot onset behavior based on molecular structure [32]. Yield sooting index (YSI) was proposed as an alternative to TSI that is based on the total soot volume fraction in a laminar co-flow diffusion flame [33] and also enables predictive evaluation of soot formation based on molecular structure. These metrics are useful in that they provide guidelines for designing fuels to meet specifications, in this case sooting propensity.

The accuracy and robustness of YSI has been shown to be promising across a wide scale of fuels and conditions [34], and can be used as a guideline for designing fuel blends with reduced sooting tendency [35]. However, recent measurements show that soot emissions from engine operating conditions correlate poorly with YSI [36]. Considering the increased complexity of the engine combustion process compared to a laminar flame, one might expect that other ignition and combustion characteristics of a fuel would need to be accounted for, for example the cetane number. Furthermore, since the YSI metric was developed under atmospheric conditions, the pressure effects remain uncertain. Numerical simulations have suggested that the YSI is robust at elevated pressures relevant to practical combustion devices [37], but these findings contradict the experimentally observed variation in pressure sensitivity of soot formation across fuels discussed previously [13–17]. Nonetheless, considering the similarities between diffusion flames and pyrolysis, it is reasonable to expect that the YSI has similar predictive capabilities for soot formation under pyrolysis.

One particular subtlety in the YSI is that it can either be defined on a

mass or mole basis. The vast majority of the YSI database is defined on a mole basis, as the mole basis is arguably more fundamental and more easily enables using molecular structure to generate rules for predicting sooting propensity [34]. However, for practical fuels, the average molecular formula may not be known precisely, making it difficult to construct a mole-based metric. In these cases, a mass-based YSI would appear to be more appropriate and was thus developed for selected diesel and jet fuels [38]. This also raises the question on the practical applicability of the two approaches for real combustion systems. Soot emissions are evaluated based on the mass or volume of fuel consumed, irrespective of whether the molecular weight is known or not, and as such a mass-based sooting index offers a more appropriate comparison.

The goal of this study is to present measurements of PAH and soot formation in high pressure fuel pyrolysis of various diesel, gasoline, selected surrogates, and related hydrocarbon fuels. The experiments were carried out by injecting a small and well-characterized amount of fuel in a constant-volume pre-burn chamber at 76 bar from 1400 to 1700 K. High-speed planar laser induced fluorescence (PLIF) and diffused back-illumination extinction imaging (DBI-EI) deliver time-resolved measurements of PAH and soot formation, respectively. The PAH and soot formation delay, the maximum soot formation rate, and the peak soot yield are compared across the different fuels as functions of temperature. We find that the surrogate fuels behave similarly to their respective target. The sooting propensities are also correlated to mass and mole-based YSIs. The soot delay is found to correlate well with the mass-based YSI, and the mass-based YSI generally correlates

better than mole-based YSI with the pyrolysis sooting tendencies. However, neither basis of YSI is a predictive metric for the pyrolysis soot yield.

2. Experimental methods

2.1. Combustion vessel

The optically accessible constant volume combustion chamber was similar to what was described in an earlier work [27] with minor modifications to accommodate laser diagnostics. A schematic of the setup is shown in Figure 1. The combustion chamber itself was identical to that used in [27], with the exception of the top and bottom ports that were replaced with custom laser-specific windows for the laser sheet to come through and exit. A damping plate was placed on the top window to block scattered laser light from the exit. The temperature in the vessel was measured by calibration with the pressure and density, since the pressure measurement has a much shorter response time than the temperature measurement from a thermocouple, and density is virtually constant throughout each injection event. The temperatures and pressures in the chamber were controlled by burning a spark-ignited premixed charge of acetylene, hydrogen, nitrogen, and oxygen, which we refer to as the pre-burn mixture. The present work employed a stoichiometric pre-burn charge resulting in a post pre-burn ambient environment containing 89.71% nitrogen, 6.52% carbon dioxide, and 3.77% water by volume. It should be noted that the conditions differ slightly from true pyrolysis as ppm levels of OH and O_2 are expected based on chemical equilibrium above 1400 K. The pre-burn mixture reaches maximum temperature of nearly 1800 K in under 200 ms. Following the pre-burn event, a cooldown period ensues

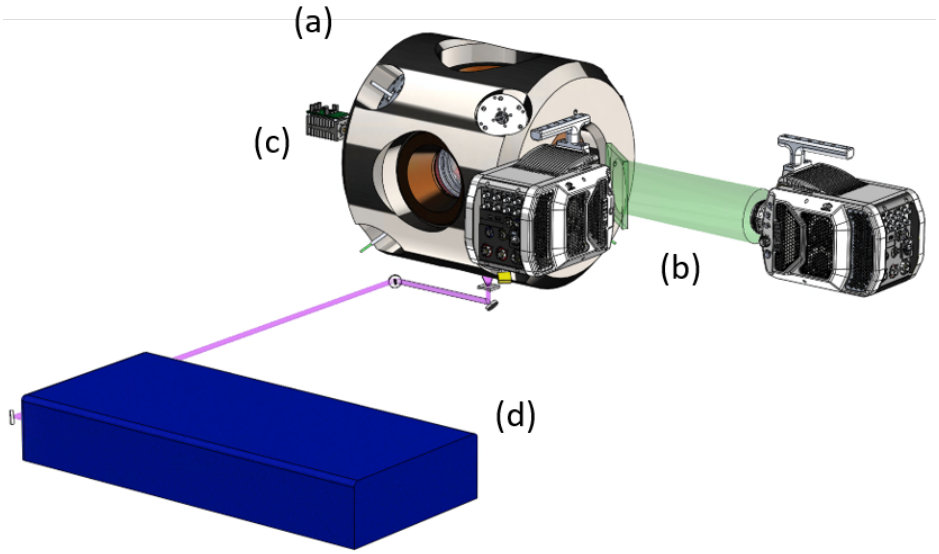

Figure 1: A schematic of the experimental setup, consisting of (a) an optically accessible constant-volume combustion vessel, (b) high-speed cameras, (c) a 520 nm LED and diffuser, and (d) a pulsed burst-mode 355 nm Nd:YAG laser.

resulting in a time-dependent range of temperatures and pressures in which the fuel spray can be injected. The chamber reaches 1700 K in about 300 ms after reaching peak temperature, and 1400 K in about 1 second, allowing for plenty of time for the pre-burn to establish chemical equilibrium. The measurements are performed up to 30 ms after injection, thus the transience of the cooldown is negligible (about 10 K over the full 30 ms). For these experiments, the target temperature ranged from 1400 to 1700 K, and the target pressure was held constant at 76 bar.

A syringe pump (Teledyne 30D) pressurized the fuel to 476 bar (400 bar pressure difference) and the injector is a Denso Spray A-3 injector with a single axial orifice with a 94 µm diameter. A short injection duration

was targeted (around 200 µs) to limit fuel penetration and the mass of fuel injected. This allows the fuel spray to remain within the field of view for a relatively long time, with parts of the fuel vapor or soot leaving the visualized area at least 25 ms after the injection.

2.2. Fuels

A total of 12 fuels were investigated in this study. RD5-87 is a regular research-grade E10 gasoline. PACE-8 and PACE-20 are two gasoline surrogate fuels from the Partnership to Advance Combustion Engines (PACE) program. *Iso*-octane (iC8), 1,2,4-trimethylbenzene (TMB), and cyclopentane (cC5) were studied as selected single-component hydrocarbons as they are major components of the PACE surrogates. CFA is a ultra-low sulfur diesel certification fuel from Chevron-Philips Chemical Co. V0a, V0b, V1, and V2 are diesel surrogates developed by Mueller and coworkers [39]. *N*-dodecane (nC12) was selected as a single-component fuel to be compared to the diesel fuels, as it is often treated as a diesel surrogate and studied under diesel conditions due to its similar physical and chemical properties to those of practical diesel fuels [40–43]. The components of the gasoline and diesel surrogate fuels are listed in Tables 1 and 2, respectively.

The estimated YSI values are listed in Table 3. Values of mole-based YSI ($\mathrm{YSI_{mole}}$) were taken from the online database from the unified scale [44] with the exception of *iso*-pentane, which was predicted from its molecular structure. Values of mass-based YSI ($\mathrm{YSI_{mass}}$) were determined experimentally from [38]. The YSI values of the gasolines are estimated from mass-based mixing rules based on the YSI values of the components, again taken from [38]. The YSI of RD5-87 is currently unknown so it is not listed. Some

Table 1: Mass fractions of gasoline surrogate fuels

Surrogate	PACE-8	PACE-20
Component name	wt%	
tetralin	0	3.9
1,2,4-trimethylbenzene	29.8	14.0
toluene	0	10.7
iso-octane	22.8	23.3
n-heptane	15.5	10.6
ethanol	10.0	10.2
1-hexene	4.9	4.9
cyclopentane	8.4	10.6
n-pentane	0	11.8
iso-pentane	8.6	0

Table 2: Mass fractions of diesel surrogate fuels

Surrogate	V0a	V0b	V1	V2
Component name	wt%			
iso-cetane	42	33	35	0
n-hexadecane	32	0	3	0
1-methylnaphthalene	15	12	11	11
decalin	11	0	4	0
n-octadecane	0	32	27	15
tetralin	0	15	11	12
1,2,4-trimethylbenzene	0	8	5	0
butylcyclohexane	0	0	4	15
1,3,5-triisopropylbenzene	0	0	0	17
1,3,5-triisopropylcyclohexane	0	0	0	13
2-methylheptadecane	0	0	0	10
perhydrophenanthrene	0	0	0	6
n-eicosane	0	0	0	1

gasoline components (ethanol, 1-hexene, cyclopentane, *n*-pentane, and *iso*-pentane) do not have a determined mass-based YSI. The mass-based YSI of these components was estimated based on the linear regression of the mass-based YSI versus the mole-based YSI divided by the molecular weight for all the compounds used in [38]. This regression is shown in Figure S1 and described by Equation S1 in the Supplementary Materials (SM). The coefficient of determination of this regression is $R^2 = 0.99$, suggesting that this is a valid estimate. In any case, the contribution of the YSI from these aforementioned components is small since the YSI of the gasolines are mostly determined by the contributions from the aromatic components, so small errors in the YSI estimates of these single components will have very little effect on the multi-component surrogates.

2.3. Image acquisition and processing

Diffuse back illuminated extinction imaging was performed using a 520-nm LED operating at 10 kHz and 300-ns long pulses in conjunction with a light-shaping optic, a field lens and an engineered diffuser. The diffuse light was collected on the other side of the optical chamber using a 50 mm f/1.2 lens equipped with a 500D close-up lens, and spectrally filtered with a 520-nm bandpass filter (36-nm bandwith). Images were collected using a Phantom v2512 high-speed camera operating at 20 kHz with 2 µs exposure time. The camera was operated at double the LED frequency to enable dynamic background subtraction and removal of broadband emission from hot soot particles at each time step. The background 2-D extinction measurements were converted into optical thickness KL using the Beer-Lambert

Table 3: Estimated YSI values for fuels used in this study

Name (abbrev.)	YSI_{mass}	YSI_{mole}
PACE8	88.6	105.3
PACE20	75.6	91.2
iC8	23.8	61.7
TMB	259	308
cC5	13.6	39.4
CFA	122	N/A
V0a	89.2	190
V0b	121	229
V1	103	208
V2	137	247
nC12	9.8	71.7

law,

$$Tr = \frac{I}{I_0} = \exp(-KL), \tag{1}$$

where Tr is the optical transmission, I is the transmitted LED intensity, I_0 is the incident intensity, K is the dimensional extinction coefficient, and L is the path length through the soot cloud. The projected soot volume fraction $pSVF$, which is the soot volume fraction integrated through the line of sight, is proportional to the optical thickness, given by

$$pSVF = \frac{\lambda}{k_e} KL, \tag{2}$$

where λ is the wavelength of the incident light (520 nm) and k_e is the non-dimensional extinction coefficient, assumed to be 7.8 [45] and has some uncertainty that will be discussed. The scaling from KL to $pSVF$ in this case is roughly a factor of 7 ppm·cm. The average soot volume fraction SVF through the line of sight is given as

$$SVF = \frac{pSVF}{L}. \tag{3}$$

The path length L can be estimated as the characteristic width of the soot field for an order-of-magnitude analysis. A more in-depth analysis to accurately determine the local soot volume fraction would require 3-dimensional information of the soot field. While there are methods to achieve this, e.g. tomographic reconstruction, such an analysis is not carried out here. The soot mass in each pixel, $m_{\text{soot, pixel}}$, scales with the projected soot volume fraction as

$$m_{\text{soot, pixel}} = pSVF \cdot \rho_{\text{soot}} \Delta A_{\text{pixel}}, \tag{4}$$

where ρ_{soot} is the soot mass density and ΔA_{pixel} is the projected pixel area. The soot mass density was assumed to be 1.8 g/cm^3 [46]. The detection

limit regarding soot mass is estimated to be on the order of half a microgram based on the signal-to-noise ratio of the imaging system.

Planar laser induced fluorescence was performed using a 355 nm pulsed burst-mode Nd:YAG laser to monitor PAH formation and distribution. A set of cylindrical lenses formed a 58-mm long laser sheet with an approximate thickness of 300 µm. Each burst fired 50 mJ pulses at 10 kHz over a 15-ms duration, for a total of 150 laser shots. The spatial energy distribution of the laser-sheet was corrected by measuring the fluorescence signal intensity distribution from formalin uniformly distributed in the chamber. A high-speed photodiode tracked the laser shot-to-shot variation to measure laser shot intensity to be used during the correction procedure. The fluorescence light was collected from the same perspective reflected to a second Phantom v2512 high-speed camera by a dichroic beam-splitter. The camera was also operated at 20 kHz, double the laser frequency, for the same reasons mentioned previously. A multi-line CH_2O filter combined with a 450 nm shortpass filter and KG3 heat absorbing glass was used to filter the fluorescence signal. The background-subtracted signal was corrected for spatial and shot-to-shot variations in intensity and spatially integrated to obtain a total PAH-LIF intensity I_{P} for each frame. This is used as a proxy for PAH concentration with arbitrary units. It is noted that this technique is selective to moderate-sized PAHs composed mainly of 3 and 4-rings aromatics that are responsive to 355 nm excitation: Smaller PAHs tend to have energy bandgaps larger than 355 nm (3.5 eV), and larger PAHs have lower fluorescence quantum yield [47].

The measurable fluorescence signal was susceptible to laser attenuation and signal trapping from soot: Both the laser excitation and fluorescence

emission were attenuated from the presence of soot. To compensate for this effect, the fluorescence intensity at each location was divided by the soot optical transmission Tr from Equation (1) to obtain an attenuation-corrected PAH-LIF intensity $I_{\mathrm{P,\,corr}}$, expressed as follows:

$$I_{\mathrm{P,\,corr}} = \frac{I_{\mathrm{P}}}{Tr}. \tag{5}$$

A more accurate correction would consider the 3D geometry of the jet and the path of the laser radiation and fluorescence emission, which would require a significantly more complex correction algorithm. This simple correction suffices for a qualitative analysis, although drawing conclusions will be limited to low and moderate soot optical thicknesses, where laser attenuation and signal trapping effects are small and the extent of the correction is less significant.

3. Results and discussion

3.1. Time evolution of PAH-LIF and soot formation

Selected false-color composite maps showing the time evolution of the PAH-LIF intensity (green) and soot optical thickness (red) in pyrolyzing sprays of iso-octane at three temperatures (1400, 1550 and 1700 K) are shown in Figure 2. The composite maps are layered such that soot optical thickness is shown over PAH-LIF intensity, and as such co-local signals are not shown. These conditions were selected to represent the low, moderate, and high temperatures explored in this study. At 1400 K, only a small amount of soot is formed and PAH-LIF intensity continuously grows. Measurement of PAH-LIF intensity is virtually unhindered by soot optical extinction. At 1550 K,

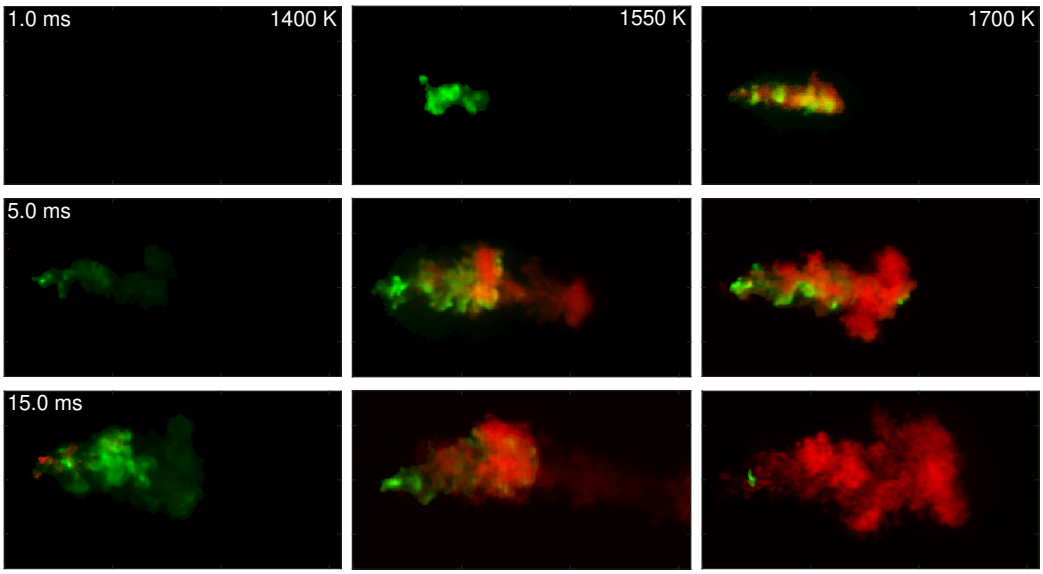

Figure 2: Examples of maps of the PAH-LIF intensity I_{P} (green) and soot optical thickness (red) from iso-octane sprays. Each row represents a selected time after the start of injection, labeled in the top-left corner of the left column. The injection duration is approximately 0.3 ms. Each column represents a selected temperature (1400, 1550, and 1700 K), labeled in the top-right corner of the top row. Each map is 62 mm across and 32 mm tall, with the injector tip located at the center of the left edge. (For interpretation of the references to color in this figure, the reader is referred to the web version of this article.)

there is PAH-LIF signal within a fraction of a millisecond after injection, and soot still takes a few milliseconds to form. Signal trapping begins to affect the PAH-LIF intensity distribution at later times. At 1700 K, soot onset is under 1 ms, and signal trapping due to soot almost completely shuts out the PAH-LIF signal all across the field but the near-nozzle region, where soot concentration remains low.

Selected false-color maps showing sample snapshots of the projected soot

volume fraction and PAH-LIF uncorrected and corrected intensities are shown in Figure 3. When the soot concentration is low, e.g. $pSVF < 5$ ppm·cm, the PAH-LIF intensity correction can reasonably recover a more reliable PAH-LIF intensity map. As the soot concentration exceeds $pSVF = 5$ ppm·cm, the correction loses accuracy and portions of the PAH-LIF signal become indistinguishable from noise. The characteristic width of the soot field is on the order of 1 cm, so assuming that the field is reasonably axisymmetric, the depth-averaged soot volume fraction (in ppm) can be estimated from Eq. 3 to be on the same order of magnitude as $pSVF$ (in ppm·cm).

The time evolutions of the spatially-integrated PAH-LIF intensities and soot masses from iso-octane sprays at 1400, 1550 and 1700 K temperatures are shown in Figure 4. At 1400 K, both PAH-LIF intensity and soot increase at a nearly constant rate after a few millisecond delay. As temperature increases, the delays for both PAH-LIF and soot formations decrease. While mild at 1400 K, the growth rate of PAH-LIF slows down around the onset of soot formation. This effect is confounded by laser attenuation and signal trapping at high temperatures, but the PAH growth rate reduction can still be observed for the 1550 K case. This reduction in PAH-LIF signal - a proxy for PAH concentration - is likely due to PAHs beginning to be converted into soot. At 1700 K, the PAH-LIF signal drops sharply as soot forms, but it is unclear how much of this is due to laser attenuation and signal trapping versus conversion to soot. The total magnitude of the PAH-LIF intensity also decreases with temperature, but again this is confounded by signal trapping.

There is a possibility that some of the PAH-LIF signal may be coincident with laser-induced incandescence (LII). However, at early times near the

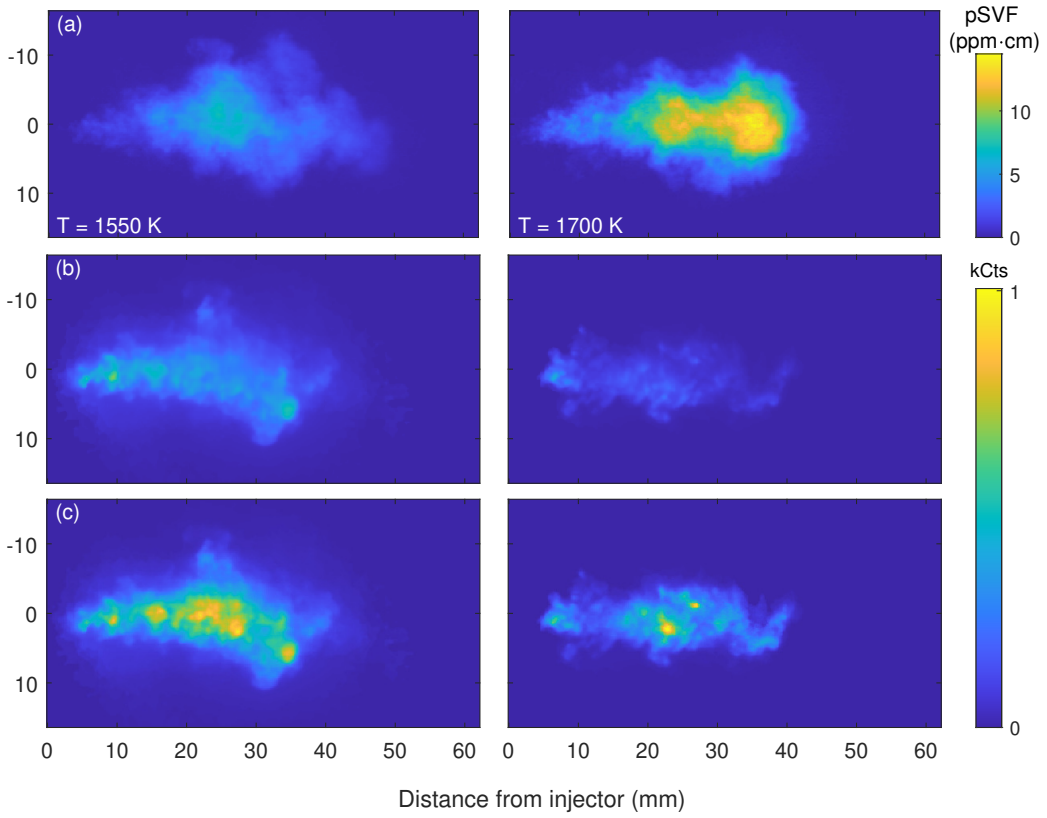

Figure 3: Selected false-color snapshots of (a) soot optical thickness KL in the top row, (b) PAH-LIF intensity I_{P} in the middle row, and (c) corrected PAH-LIF intensity $I_{\mathrm{P,\,corr}}$ in the bottom row from an iso-octane spray 7 ms after the start of injection. The left column is at 1550 K and the right column is at 1700 K. (For interpretation of the references to color in this figure, the reader is referred to the web version of this article.)

PAH-LIF onset and at low temperatures, there is little to no soot. Since LII signal would scale with soot concentration, the PAH-LIF signal under these conditions would not be affected by LII. Furthermore, the PAH-LIF signal tends to decrease with increasing soot concentration (due to signal trapping or conversion to larger PAHs or soot), which would therefore behave opposite to LII signal intensity. In fact, the strongest PAH-LIF signal generally comes from the 1400 K and 1450 K conditions where PAHs can form with minimal conversion to soot. Thus, we believe that LII does not represent a relevant contribution to the measured signal in these measurements.

The total soot mass increases with temperature, eventually plateauing at the highest temperatures. The slight decrease in soot mass at the end of the 1700 K measurement is due to instances of soot leaving the field of view. There may also be a small effect from oxidation of soot due to the leftover oxygen species from the pre-burn, estimated to be on the order of 10 ppm from equilibrium calculations. That being said, the reaction timescale from such a small amount of oxygen is estimated to be on the order of seconds based on experiments performed in the same setup with small (1-5%) amounts of O_2, where the oxidation timescale is milliseconds [48]. Thus, soot oxidation is an unlikely factor here.

3.2. Fuel and temperature dependence of PAH-LIF and soot formation

To condense and summarize the data across the different fuels and temperatures investigated, we report the PAH-LIF and soot onset delay, the maximum formation rate, and the peak yield, for each fuel as a function of temperature. The PAH-LIF onset delays are shown in Figure 5. There is a clear distinction between fuels with or without aromatic species. The PAH-

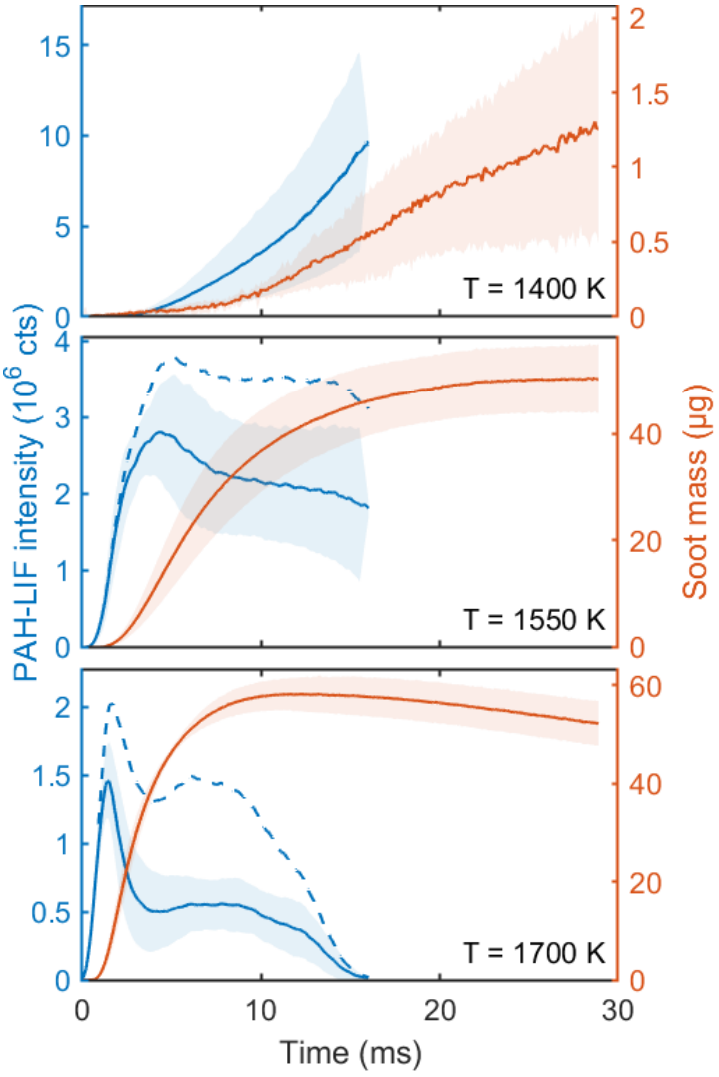

Figure 4: Time traces of the integrated PAH-LIF intensity I_p (blue solid line), corrected PAH-LIF intensity $I_{\mathrm{P,\ corr}}$ (blue dashed line), and soot mass (orange line) at 1400, 1550, and 1700 K from iso-octane sprays. The time is measured relative to the start of injection. The lines are the mean and the shaded area represents the standard error of the mean with a 95% confidence interval. PAH-LIF is measured for up to 16 ms, and soot mass is measured for up to 30 ms.

LIF delay of the pure alkane fuels (iso-octane, cyclopentane, and n-dodecane) lags the delay of the aromatic fuels by up to an order of magnitude, in particular at lower temperatures. This is unsurprising, as aromatic-containing fuels effectively have a head-start in the fuel-to-PAH formation pathway compared to non-aromatic fuels. In the case of the CFA and the diesel surrogates, the measurement of PAH-LIF delay is confounded by fuel fluorescence and the observed PAH-LIF delay is virtually instantaneous at all temperatures. In these cases, the measured PAH-LIF delay is not meaningful as it largely a measure of fuel fluorescence. One interesting note is that fuel fluorescence from CFA is much stronger than that from any of its surrogates. The only component of the diesel surrogate fuels expected to emit fluorescence with 355 nm excitation is 1-methylnaphthalene. This may suggest that CFA diesel contains other multi-ring aromatics that are sensitive to 355 nm excitation. For RD5-87 and the PACE surrogates, there is very weak temperature dependence of the PAH-LIF delay, which suggests that the formation of PAHs from the aromatics in the fuel is fast and largely insensitive to this temperature range. The PAH-LIF delay of the alkanes exhibits a clear temperature dependence as the fuel must break down into aromatic precursors such as acetylene and propargyl before PAHs can form.

The maximum formation rate and peak yield of the PAH-LIF signal are shown in Figure 5. Only the data from 1400 and 1450 K are shown as the soot concentrations at this temperature are low enough such that signal trapping is manageable. The maximum formation rate increases with temperature for every fuel as expected. The peak yield for most fuels also increases with temperature, although relatively not as much as the rate, and there are some

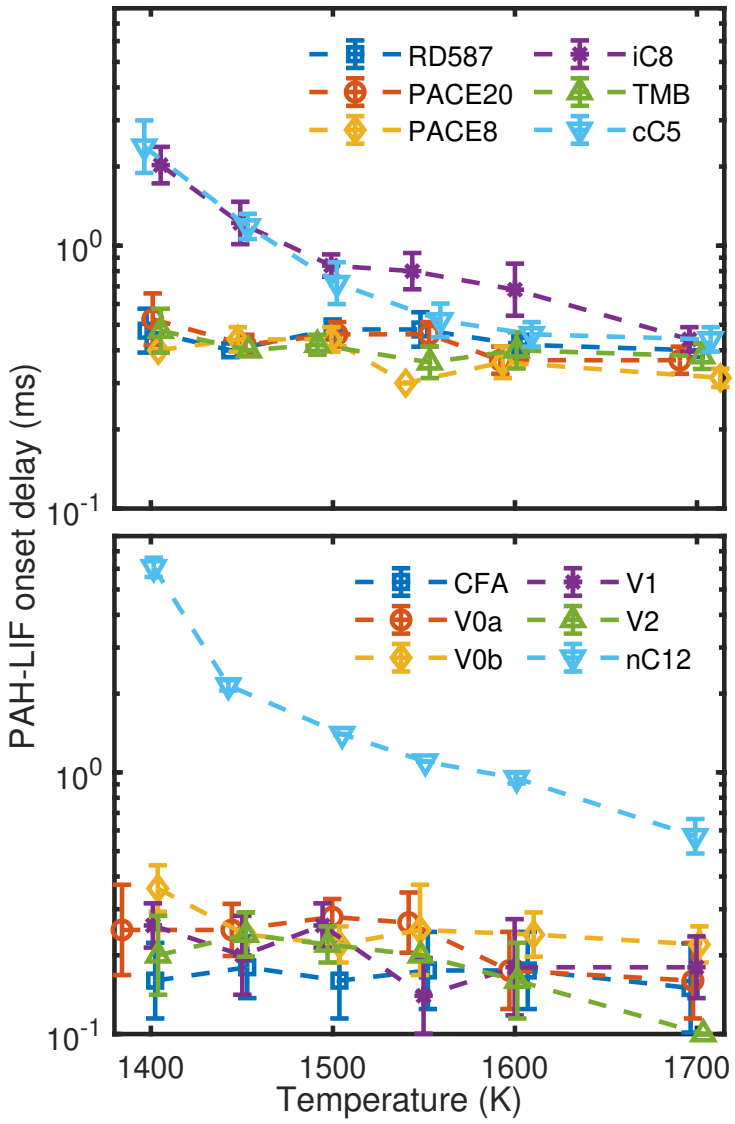

Figure 5: Measurements of PAH-LIF onset delays of the fuels. The fuels have been separated into their groups based on their relevance to gasoline or diesel for clarity. The symbols represent the mean and error bars represent the geometric standard error of the mean with a 95% confidence interval. The dashed lines are interpolations between the data points and are drawn to guide the eye. The lowest value on the y-axis (0.1 ms) reflects the sampling rate of the data acquisition.

instances where the peak yield is lower at 1450 K than at 1400 K. The reduced yield with increasing temperature is likely due to conversion of these 3-4 ring PAHs that are sensitive to 355 nm excitation into larger PAHs that are less responsive to 355 nm excitation, or even soot. Another consideration is that the fluorescence quantum yield of PAHs may decrease with increasing temperature [49]. For all fuels at temperatures above 1450 K, the peak PAH-LIF yields continue to decrease with temperature, although this effect becomes confounded with signal trapping and as such are not shown here. The alkanes also exhibit the strongest temperature sensitivity, consistent with the results shown in Figure 5, with mostly a factor of at least 2 increase in PAH-LIF rate and yield from 1400 and 1450 K. In particular, *n*-dodecane has over a factor of 10 increase in PAH-LIF rate and yield from 1400 and 1450 K. The stronger sensitivity of the PAH-LIF growth and yield to temperature between 1400 and 1450 K from *n*-dodecane compared to the other alkanes (*iso*-octane and cyclopentane) may indicate notable differences in the fuel-to-PAH pathway that arise from differences in fuel molecular structure. For example, the side methyl groups on *iso*-octane may break off and form methyl radicals more easily than *n*-dodecane. This is indeed observed when comparing pyrolysis of *iso*-octane and *n*-heptane in shock tubes [50]. Perhaps the immediate radicals formed from *iso*-octane pyrolysis can more readily form PAHs than those from *n*-dodecane. The analogy is not as obvious with cyclopentane, but the data suggests a similar conclusion, i.e. the immediate pyrolysis products of cyclopentane may more readily form PAHs. The PAH-LIF rate and yield of the other fuels at the two temperatures are mostly within a factor of less than 1.5 with a few exceptions.

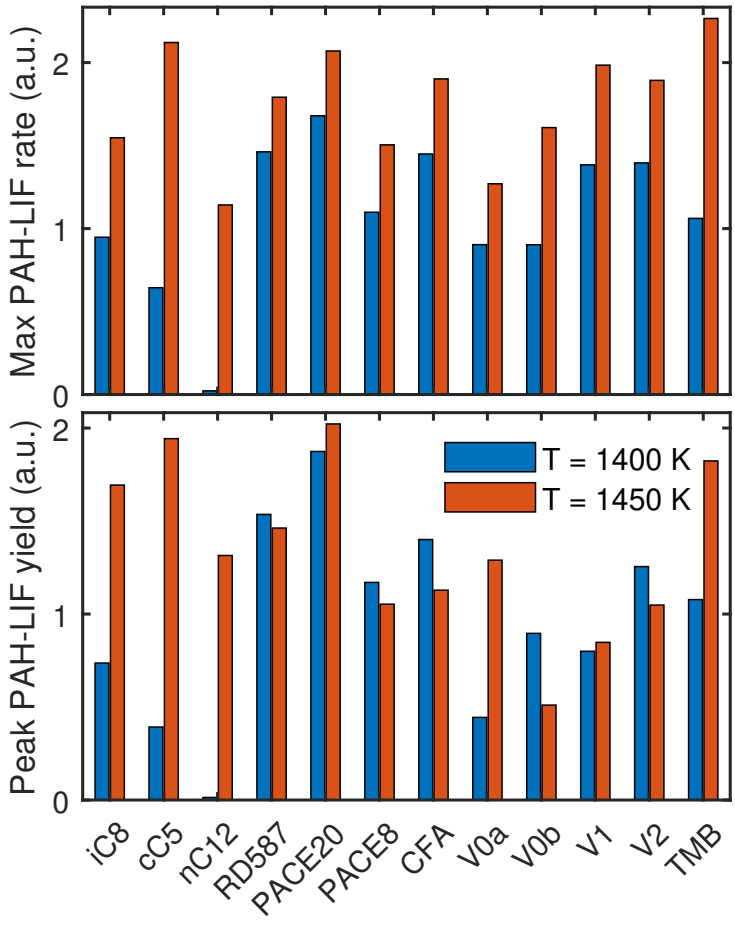

Figure 6: Measurements of the PAH-LIF maximum formation rate (top) and peak yield (bottom), normalized by the injected mass of fuel, at 1400 and 1450 K. The fuels are sorted into groups of alkanes, gasolines, diesels, and TMB.

The soot onset delays for all fuels and temperature conditions are summarized in Figure 7. As expected, the delay decreases with increasing temperature for all fuels. The difference in delay between non-aromatic and aromatic fuels is less pronounced, roughly a factor of three at most. This is likely due to PAH-to-soot chemical pathways across different fuels being less distinguishable than the fuel-to-PAH pathways, i.e. a common mechanism of soot formation from PAHs [25] and fuel molecular structure being influential primarily during the early stages of soot growth [51]. Most of the fuels have a measurable soot delay at 1400 K, except for V0a, V2, and *n*-dodecane, for which there is no detectable soot within the 30 ms observation period. The soot delay for trimethylbenzene is notably faster than any of the other fuels. This is likely because this fuel is an aromatic and can be considered a precursor to PAHs and thus soot, meaning that it has a favorable chemical structure to quickly form soot. The other multi-component fuels have some aromatic content, but are still predominantly non-aromatic compounds in terms of overall mass. This means it will take them a slightly longer time to form enough PAHs to evolve into soot.

The maximum soot formation rates, normalized by the respective injected masses of carbon, are shown in Figure 8. These represent the fraction of carbon that is converted into soot, per millisecond. Most of the fuels behave similarly: while the non-aromatic fuels in general have a slightly lower maximum formation rate, the difference is not as noticeable. This reflects the weak sensitivity of PAH-to-soot chemical pathways to fuels. The main exception is trimethylbenzene, which has the fastest maximum soot formation rate simply because it is a neat aromatic, as discussed above.

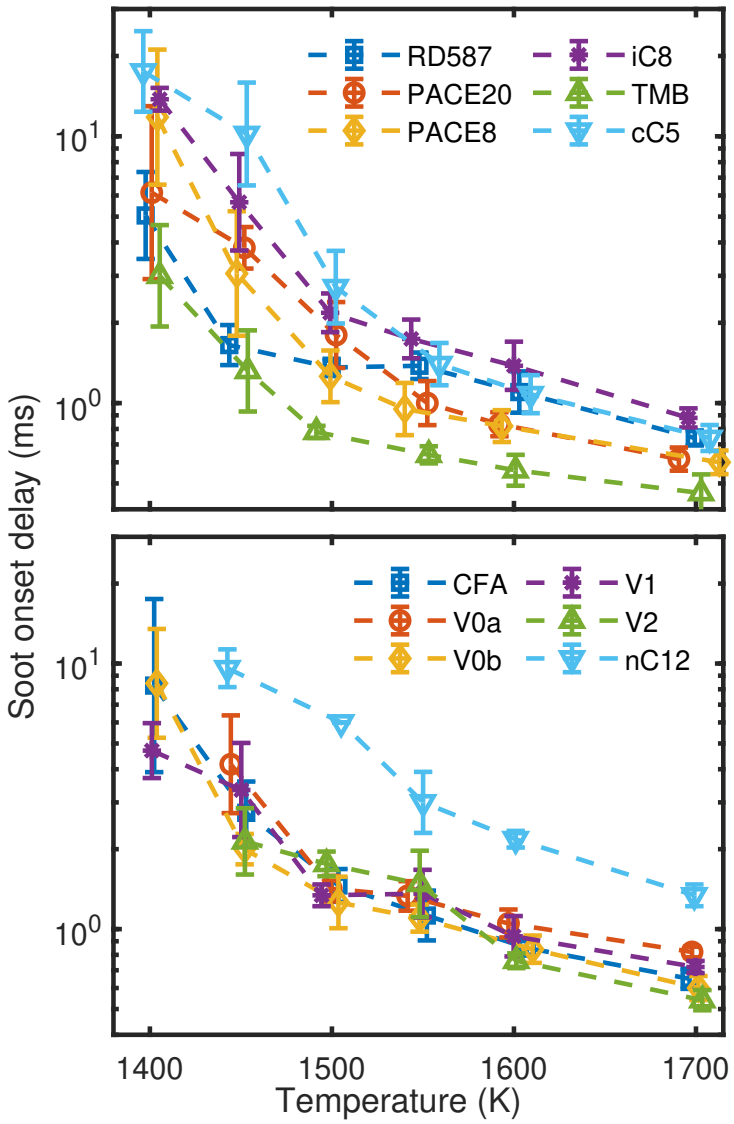

Figure 7: Measurements of soot onset delays of the fuels. The symbols represent the mean and error bars represent the standard error with a 95% confidence interval. The dashed lines are interpolations between the data points and are drawn to guide the eye.

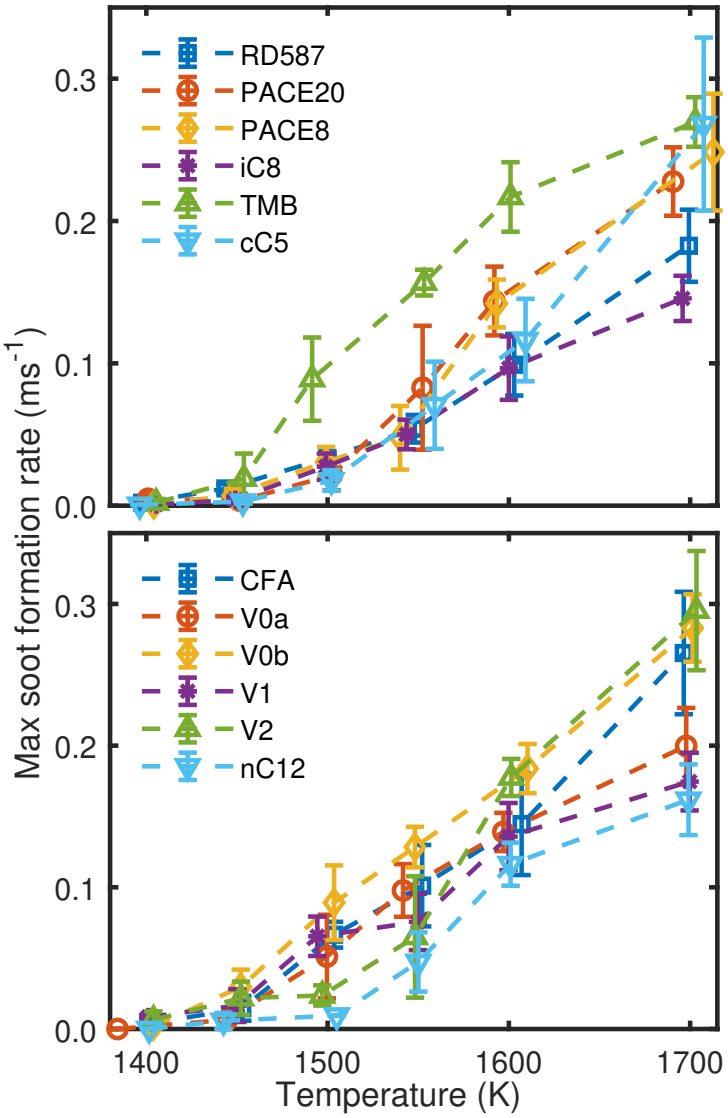

Figure 8: Measurements of the maximum soot formation rate, normalized by the injected mass of carbon. The y-values represent the fraction of injected carbon converted into soot per millisecond. The symbols represent the mean and error bars represent the standard error of the mean with a 95% confidence interval. The dashed lines are interpolations between the data points and are drawn to guide the eye.

The maximum soot yields, or the measured soot masses divided by injected carbon masses, are shown in Figure 9. At lower temperatures, the maximum soot yields may be throttled by the limited observation time of 30 ms, at which point the slow increase in soot mass still appears to be happening (c.f. Fig. 4). At higher temperatures, the pyrolyzing fuel is able to reach a quasi-steady-state condition where the soot mass has finished increasing, and the maximum yield is typically achieved by 20 ms. Most of the fuels convert between 60 to 80% of their carbon mass into soot except for *iso*-octane and cyclopentane, which convert just under half of their carbon mass into soot. The shape of the curves have some features of autocatalytic behavior: The soot yield initially increases with temperature and then plateaus in a characteristic S-shape curve [24]. A key difference between these pyrolyzing sprays and the shock tube experiments is the extended observation time in the present tests: Shock tube experiments are generally limited to a few milliseconds, while these experiments are carried out for 30 ms. This allows more time for soot formation to approach a quasi-steady state. The time-based soot yield reaches a plateau, with the plateau level reached earlier at higher temperatures, as seen in Figure 4. The variation in soot yield across fuels is thus much less than what is observed in shock tube pyrolysis [51] since the residence time no longer throttles the soot yield for any of the fuels.

One major source of uncertainty that can affect these measurements lies in the optical properties of the soot particles. The soot optical properties were assumed to be identical from all fuels at all conditions, but it is known that they can vary by more than 20% across fuels [52], and these differences may be attributed to differences in soot nano-structure and composition [53].

For example, it may be possible that the soot from *iso*-octane and cyclopentane is less mature or graphitic than soot from the other fuels. Conversely, soot from trimethylbenzene may be more graphitic or have a lower hydrogen-to-carbon (H/C) ratio considering that trimethylbenzene starts with a lower H/C ratio (1.3) compared to the gasoline or alkane fuels (∼2). These could result in the soot from *iso*-octane and cyclopentane featuring a small extinction cross-section, thus the perceived amount of soot formed appears to be less than from the other fuels. In fact, one might expect that most of the carbon under these pyrolysis conditions would tend towards the same final thermodynamic state in some form of solid carbon phase. For example, at 1700 K, roughly half of the carbon mass in *iso*-octane is measured to convert into soot and the soot mass plateaus by 15 ms, as seen in Fig 4. As such, the pyrolysis process should have reached a near-equilibrium state, yet it is unlikely that the entire other half of carbon mass does not condense, as solid carbon is far more thermodynamically favorable than gas-phase carbon at this temperature and pressure, with or without the presence of hydrogen. Resolving the uncertainty in optical properties will be necessary to more accurately understand the differences in soot formation across fuels.

3.3. Correlations with yield sooting indices

To evaluate the predictive capabilities of the YSI with sooting pyrolysis behavior, the soot measurements shown previously (delay, maximum formation rate, and maximum yield) can be correlated with either $\mathrm{YSI_{mass}}$ or $\mathrm{YSI_{mole}}$ of each fuel at each temperature. The inverse soot delay was selected over the soot delay as soot delay is typically inversely proportional to soot formation. The correlation between soot yield and $\mathrm{YSI_{mass}}$ is shown in the

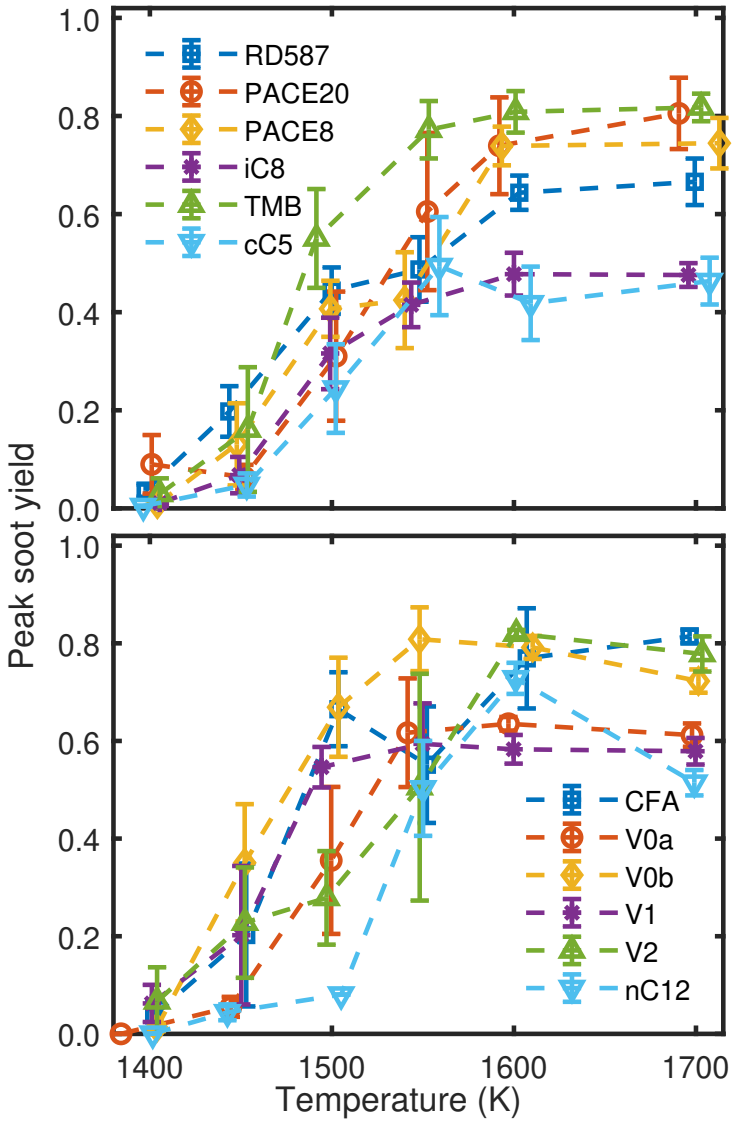

Figure 9: Measurements of the peak soot mass formed, normalized by the injected mass of carbon. The y-values represent the fraction of injected carbon converted into soot. The symbols represent the mean and error bars represent the standard error. The dashed lines are interpolations between the data points and are drawn to guide the eye.

top panel of Figure 10 as an example. The coefficient of determination of the linear regression R^2 is labeled in the top left. While the soot yield generally tends to increase with YSI, the correlation is weak. The R^2 values for all of the correlations are shown in the bottom panel of Figure 10. Only correlations at 1500 K or above were examined; the correlations at 1400 and 1450 K were omitted since they are too close to the soot onset temperature. The inverse soot delay correlates decently well with YSI_{mass} (2nd group of bars), with its lowest R^2 value at 0.7, and its average (green transparent bar) at almost 0.8. The other soot measurements (maximum formation rate and maximum yield) generally do not correlate particularly well with either YSI basis, with a few exceptions.

The strength of the correlations generally decreases from delay to rate to yield. Even though maximum soot yield might appear to be the most consistent with the definition of YSI (based on maximum soot volume fraction), they do not correlate well here considering the vastly different conditions: The maximum yield here is determined after up to 30 ms in a high pressure pyrolyzing spray, while YSI is determined in an atmospheric diffusion flame where the soot residence time is generally a few ms and may eventually be oxidized downstream. The pyrolysis soot yield here represents a near-equilibrium state where there are mostly no soot formation nor destruction reactions occurring and the time profiles of soot mass plateau. In contrast, the maximum soot volume fraction in a diffusion flame is in a transient state and occurs when the soot production rate is dynamically balanced by the soot oxidation rate as oxygen diffuses into the fuel stream. As such, YSI is more consistent with the kinetics (e.g. soot delay) involved with soot forma-

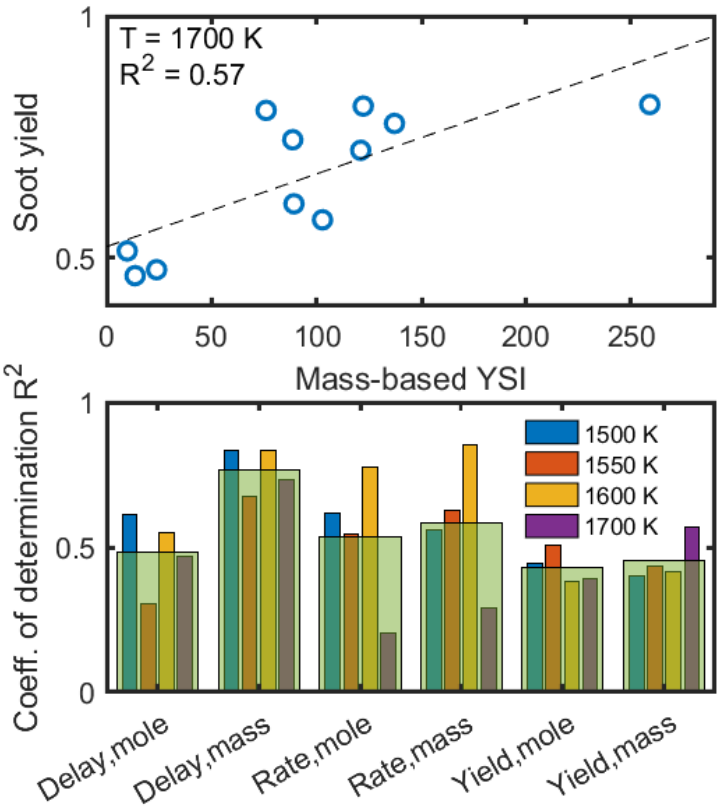

Figure 10: Top: Correlation between soot yield and YSI_{mass} at 1700 K, shown as an example. Bottom: Comparison of selected R^2 values of the correlations of inverse soot delay, maximum formation rate, or maximum soot yield with YSI_{mass} or YSI_{mole}. The mean of each group is shown by the transparent green bar that spans all bars in each group. The groups are labeled by which quantity is being correlated with which YSI basis. For example, "Rate,mole" refers to the correlation of the maximum soot formation rate with the unified mole-based YSI. (For interpretation of the references to color in this figure, the reader is referred to the web version of this article.)

tion from these pyrolysis conditions, but YSI alone is an insufficient metric to predict soot yield. The effect of pressure is unknown and may play a role here as well. As discussed earlier, YSI was developed under atmospheric conditions, and experimental evidence suggests that YSI may not be relevant at elevated pressures up to 10 bar for some select single-component hydrocarbon fuels [16, 17]. While data on the pressure effect on YSI is currently limited, it is reasonable to suspect that the elevated pressures used in this study (60 bar) limit the reliability of YSI as a predictive metric.

The soot formation process in real engines is considerably more complicated than the pyrolysis conditions investigated here. In real engines, the fuel combusts in an oxidizing environment, and ignition properties (e.g. cetane number, ignition delay, and lift-off length) of the fuel will play a role in soot formation. For example, if the ignition delay is slow or the lift-off length is long, there is effectively less residence time for soot chemistry to progress, which would inhibit soot emissions. These fuel properties are also expected to affect soot formation that YSI alone will be insufficient to describe. This has been corroborated by recent measurements of soot emissions from engine operating conditions, where soot measurements correlated poorly with YSI [36]. Both gasoline and diesel engines operate under reacting conditions, but the pyrolysis process is particularly relevant for gasoline combustion and spark-ignition engines since a large portion of soot emissions from gasoline engines come during cold-start pyrolysis of the deposited liquid fuel film, as mentioned earlier [22]. For diesel and compression-ignition engines, the fuel's ignition characteristics are expected to have a stronger influence on the sooting propensity.

Lastly, it should be noted that the correlations using the YSI_{mass} are generally stronger than the correlations using the YSI_{mole}, most notably for soot delay and only marginally for maximum soot formation rate and yield. This is consistent with the expectation that a mass-based index should be more suitable for describing soot formation across different fuels where there can be a large difference in molecular weight. In particular, CFA and its surrogates have a significantly higher molecular weights than RD5-87 and the gasoline surrogate fuels (a factor of ∼2), but have very similar pyrolysis sooting tendencies. YSI_{mass} is thus a superior predictor of soot formation via pyrolysis compared to the YSI_{mole} by itself. The mole-basis, however, remains useful in that it streamlines the use of fuel molecular structure to predict YSI. Considering that the YSI_{mole} divided by molecular weight correlates nearly perfectly with the YSI_{mass} ($R^2 = 0.99$, shown in Figure S1), this quantity can be used in lieu of a YSI_{mass}.

4. Summary and conclusions

Time-resolved soot and PAH formation were measured in high-pressure pyrolyzing sprays from a gasoline, diesel, and related single-component hydrocarbon fuels from 1400 to 1700 K at 60 bar. Soot mass was measured via optical thickness using DBI. PAH levels were measured with LIF at 355 nm as a PAH-LIF intensity and compensated for signal trapping from soot optical extinction. The delay, the maximum formation rate, and yield of PAH-LIF intensity and soot were measured at each condition for all fuels. The delays generally decreased with increasing temperature. The PAH-LIF and soot delay of the aromatic-free fuels (*iso*-octane, cyclopentane, *n*-dodecane) no-

tably lagged those of the aromatic-containing fuels. Maximum formations rates and yields of PAH-LIF and soot generally increased with temperature, with features of autocatalytic behavior. Some decrease in PAH-LIF apparent yield with temperature may be either due to PAH growth into larger molecules less sensitive to the diagnostic, conversion to soot, increased signal trapping and thermal quenching. The peak soot yield varied between 50 to 80 % of the injected carbon mass at the highest temperatures. The data collected from these experiments can be useful towards improving our understanding of PAH chemistry and soot formation at these engine relevant conditions and enable comparisons towards model predictions. While the PAH-LIF measurements here are not direct concentration measurements of any particular species, they can still be used as indicators of the presence of 3-4 ring PAHs. Some uncertainty also remains regarding variation in the optical properties of soot from the different fuels.

The soot delay, maximum formation rate, and yield were correlated with the mass and mole bases of YSI to evaluate YSI as a metric to predict sooting propensity. The soot delay correlated reasonably well with the mass-based YSI, indicating that YSI reasonably captures the kinetics of soot formation under high pressure pyrolysis. However, neither basis of YSI correlated well with soot yield. This reflects how the definition of maximum soot yield under diffusion flames represents a dynamic state where the kinetics of soot formation are balanced by that of oxidation. On the other hand, the maximum soot yield in these pyrolysis experiments occurs in a near-equilibrium state with virtually no formation nor destruction reactions occurring. As such, YSI alone is insufficient to predict soot yield under high pressure pyrolysis

on timescales of over 10 ms. The applicability of YSI at elevated pressures also remains uncertain. The mass-based YSI is also generally a better predictor than mole-based YSI. This is simply because if soot mass is the target of the metric, the metric itself should be mass-based to compensate for differences in molecular weight. The mole-based YSI divided by molecular weight serves as an excellent estimate for mass-based YSI if the mass-based YSI is not known. In the context of real engines under reacting conditions, ignition properties will also affect sooting propensity that will need to be accounted for in a soot metric.

Acknowledgements

The authors acknowledge Tyler Strickland for assistance in proofreading the article. The experiments were conducted at the Combustion Research Facility, Sandia National Laboratories, Livermore, CA. Sandia National Laboratories is a multi-mission laboratory managed and operated by national Technology and Engineering Solutions of Sandia, LLC., a wholly owned subsidiary of Honeywell International, Inc., for the U.S. Department of Energy's National Nuclear Security Administration under contract DE-NA0003525.

References

[1] B. S. Haynes, H. G. Wagner, Soot formation, Prog. Energy Combust. 7 (1981) 229–273.

[2] W. L. Chameides, M. Bergin, Soot takes center stage, Science 297 (2002) 2214–2215.

[3] W. J. Pitz, C. J. Mueller, Recent progress in the development of diesel surrogate fuels, Prog. Energy Combust. 37 (2011) 330–350.

[4] H. Richter, S. Granata, W. H. Green, J. B. Howard, Detailed modeling of PAH and soot formation in a laminar premixed benzene/oxygen/argon low-pressure flame, P. Combst. Inst. 30 (2005) 1397–1405.

[5] Y. Wang, A. Raj, S. H. Chung, A PAH growth mechanism and synergistic effect on PAH formation in counterflow diffusion flames, Combust. Flame 160 (2013) 1667–1676.

[6] N. A. Slavinskaya, U. Riedel, S. B. Dworkin, M. J. Thomson, Detailed numerical modeling of PAH formation and growth in non-premixed ethylene and ethane flames, Combust. Flame 159 (2012) 979–995.

[7] H. Böhm, D. Hesse, H. Jander, B. Lüers, J. Pietscher, H. Wagner, M. Weiss, The influence of pressure and temperature on soot formation in premixed flames, Symp. (Int.) Combust. 22 (1989) 403–411.

[8] M. Bönig, C. Feldermann, H. Jander, B. Lüers, G. Rudolph, H. G. Wagner, Soot formation in premixed C_2H_4 flat flames at elevated pressure, Symp. (Int.) Combust. 23 (1991) 1581–1587.

[9] A. E. Karataş, Ö. L. Gülder, Soot formation in high pressure laminar diffusion flames, Prog. Energy Combust. 38 (2012) 818–845.

[10] V. G. Knorre, D. Tanke, T. Thienel, H. G. Wagner, Soot formation in the pyrolysis of benzene/acetylene and acetylene/hydrogen mixtures at high carbon concentrations, Symp. (Int.) Combust. 26 (1996) 2303–2310.

[11] H. Böhm, H. Jander, D. Tanke, PAH growth and soot formation in the pyrolysis of acetylene and benzene at high temperatures and pressures: Modeling and experiment, Symp. (Int.) Combust. 27 (1998) 1605–1612.

[12] H. Kellerer, R. Koch, S. Wittig, Measurements of the growth and coagulation of soot particles in a high-pressure shock tube, Combust. Flame 120 (2000) 188–199.

[13] Ö. L. Gülder, G. Intasopa, H. I. Joo, P. M. Mandatori, D. S. Bento, M. E. Vaillancourt, Unified behaviour of maximum soot yields of methane, ethane and propane laminar diffusion flames at high pressures, Combust. Flame 158 (2011) 2037–2044.

[14] A. E. Karataş, Ö. L. Gülder, Dependence of sooting characteristics and temperature field of co-flow laminar pure and nitrogen-diluted ethylene–air diffusion flames on pressure, Combust. Flame 162 (2015) 1566–1574.

[15] E. A. Griffin, Ö. L. Gülder, Soot formation in diluted laminar ethene, propene and 1-butene diffusion flames at elevated pressures, Combust. Flame 197 (2018) 378–388.

[16] A. E. Daca, Ö. L. Gülder, Soot formation characteristics of diffusion flames of methane doped with toluene and n-heptane at elevated pressures, P. Combust. Inst. 36 (2017) 737–744.

[17] S. S. Yang, Ö. L. Gülder, Effects of benzene, cyclo-hexane and n-hexane addition to methane on soot yields in high-pressure laminar diffusion flames, P. Combust. Inst. 38 (2021) 1107–1114.

[18] H. Sabbah, L. Biennier, S. J. Klippenstein, I. R. Sims, B. R. Rowe, Exploring the role of PAHs in the formation of soot: Pyrene dimerization, J. Phys. Chem. Lett. 1 (2010) 2962–2967.

[19] H. Wang, Formation of nascent soot and other condensed-phase materials in flames, P. Combust. Inst. 33 (2011) 41–67.

[20] B. A. Adamson, S. A. Skeen, M. Ahmed, N. Hansen, Nucleation of soot: experimental assessment of the role of polycyclic aromatic hydrocarbon (PAH) dimers, Z. Phys. Chem. 234 (2020) 1295–1310.

[21] K. Johansson, M. Head-Gordon, P. Schrader, K. Wilson, H. Michelsen, Resonance-stabilized hydrocarbon-radical chain reactions may explain soot inception and growth, Science 361 (2018) 997–1000.

[22] F. Schulz, J. Schmidt, A. Kufferath, W. Samenfink, Gasoline wall films and spray/wall interaction analyzed by infrared thermography, SAE Int. J. Eng. 7 (2014) 1165–1177.

[23] M. Frenklach, S. Taki, M. Durgaprasad, R. Matula, Soot formation in shock-tube pyrolysis of acetylene, allene, and 1, 3-butadiene, Combust. Flame 54 (1983) 81–101.

[24] M. Frenklach, S. Taki, R. Matula, A conceptual model for soot formation in pyrolysis of aromatic hydrocarbons, Combust. Flame 49 (1983) 275–282.

[25] A. Gomez, M. G. Littman, I. Glassman, Comparative study of soot formation on the centerline of axisymmetric laminar diffusion flames: fuel and temperature effects, Combust. Flame 70 (1987) 225–241.

[26] K. Saito, A. Gordon, F. Williams, W. Stickle, A study of the early history of soot formation in various hydrocarbon diffusion flames, Combust. Sci. Technol. 80 (1991) 103–119.

[27] S. A. Skeen, K. Yasutomi, Measuring the soot onset temperature in high-pressure n-dodecane spray pyrolysis, Combust. Flame 188 (2018) 483–487.

[28] J. Kent, A quantitative relationship between soot yield and smoke point measurements, Combust. Flame 63 (1986) 349–358.

[29] R. A. Hunt, Relation of smoke point to molecular structure, Ind. Eng. Chem. 45 (1953) 602–606.

[30] Ö. L. Gülder, Influence of hydrocarbon fuel structural constitution and flame temperature on soot formation in laminar diffusion flames, Combust. Flame 78 (1989) 179–194.

[31] ASTM D1322-15e1, Standard test method for smoke point of kerosene and aviation turbine fuel, ASTM Int., West Conshohocken, PA, 2015.

[32] H. Calcote, D. Manos, Effect of molecular structure on incipient soot formation, Combust. Flame 49 (1983) 289–304.

[33] C. S. McEnally, L. D. Pfefferle, Improved sooting tendency measurements for aromatic hydrocarbons and their implications for naphthalene formation pathways, Combust. Flame 148 (2007) 210–222.

[34] D. D. Das, P. C. S. John, C. S. McEnally, S. Kim, L. D. Pfefferle, Measuring and predicting sooting tendencies of oxygenates, alkanes, alkenes,

cycloalkanes, and aromatics on a unified scale, Combust. Flame 190 (2018) 349–364.

[35] H. Kwon, S. Lapointe, K. Zhang, S. W. Wagnon, W. J. Pitz, J. Zhu, C. S. McEnally, L. D. Pfefferle, Y. Xuan, Sooting tendencies of 20 bio-derived fuels for advanced spark-ignition engines, Fuel 276 (2020) 118059.

[36] C. Mueller, J. Manin, L. Pickett, "Heavy-Duty Mixed-Controlled Compression Ignition: Fuel Effects and Ducted Fuel Injection." Presentation at U.S. Department of Energy Vehicle Technologies Office 2020 Annual Merit Review.

[37] H. Kwon, A. Jain, C. S. McEnally, L. D. Pfefferle, Y. Xuan, Numerical investigation of the pressure-dependence of yield sooting indices for n-alkane and aromatic species, Fuel 254 (2019) 115574.

[38] D. D. Das, C. S. McEnally, T. A. Kwan, J. B. Zimmerman, W. J. Cannella, C. J. Mueller, L. D. Pfefferle, Sooting tendencies of diesel fuels, jet fuels, and their surrogates in diffusion flames, Fuel 197 (2017) 445–458.

[39] C. J. Mueller, W. J. Cannella, T. J. Bruno, B. Bunting, H. D. Dettman, J. A. Franz, M. L. Huber, M. Natarajan, W. J. Pitz, M. A. Ratcliff, et al., Methodology for formulating diesel surrogate fuels with accurate compositional, ignition-quality, and volatility characteristics, Energ. Fuels 26 (2012) 3284–3303.

[40] S. S. Pandurangi, M. Bolla, Y. M. Wright, K. Boulouchos, S. A. Skeen, J. Manin, L. M. Pickett, Onset and progression of soot in high-pressure

n-dodecane sprays under diesel engine conditions, Int. J. Engine Res. 18 (2017) 436–452.

[41] T. Yao, Y. Pei, B.-J. Zhong, S. Som, T. Lu, K. H. Luo, A compact skeletal mechanism for n-dodecane with optimized semi-global low-temperature chemistry for diesel engine simulations, Fuel 191 (2017) 339–349.

[42] Z. Luo, S. Som, S. M. Sarathy, M. Plomer, W. J. Pitz, D. E. Longman, T. Lu, Development and validation of an n-dodecane skeletal mechanism for spray combustion applications, Combust. Theor. Model. 18 (2014) 187–203.

[43] C. Gong, M. Jangi, X.-S. Bai, Large eddy simulation of n-dodecane spray combustion in a high pressure combustion vessel, Appl. Energ. 136 (2014) 373–381.

[44] C. S. McEnally, D. D. Das, L. D. Pfefferle, Yield Sooting Index Database Volume 2: Sooting Tendencies of a Wide Range of Fuel Compounds on a Unified Scale (2017). doi:10.7910/DVN/7HGFT8.
URL https://doi.org/10.7910/DVN/7HGFT8

[45] S. A. Skeen, K. Yasutomi, E. Cenker, B. Adamson, N. Hansen, L. M. Pickett, Standardized optical constants for soot quantification in high-pressure sprays, SAE Int. J. Eng. 11 (2018) 805–816.

[46] M. Choi, G. W. Mulholland, A. Hamins, T. Kashiwagi, Comparisons of the soot volume fraction using gravimetric and light extinction techniques, Combust. Flame 102 (1995) 161–169.

[47] S. Bejaoui, X. Mercier, P. Desgroux, E. Therssen, Laser induced fluorescence spectroscopy of aromatic species produced in atmospheric sooting flames using UV and visible excitation wavelengths, Combust. Flame 161 (2014) 2479–2491.

[48] S. A. Skeen, L. M. Pickett, E. Cenker, K. Yasutomi, "Soot Formation in Spray Pyrolysis: Effects of Ambient Temperature, Oxygen Concentration, and Fuel." Presentation at the Advanced Engine Combustion Program Review (2018).

[49] Y. Zhang, L. Wang, P. Liu, Y. Li, R. Zhan, Z. Huang, H. Lin, Measurement and extrapolation modeling of pah laser-induced fluorescence spectra at elevated temperatures, Appl. Phys. B 125 (2019) 1–12.

[50] D. F. Davidson, M. Oehlschlaeger, R. K. Hanson, Methyl concentration time-histories during iso-octane and n-heptane oxidation and pyrolysis, Proc. Combust. Inst. 31 (2007) 321–328.

[51] M. Frenklach, D. W. Clary, W. C. Gardiner Jr, S. E. Stein, Effect of fuel structure on pathways to soot, Symp. (Int.) Combust. 21 (1988) 1067–1076.

[52] I. Colbeck, B. Atkinson, Y. Johar, The morphology and optical properties of soot produced by different fuels, J. Aerosol Sci. 28 (1997) 715–723.

[53] M. Alfè, B. Apicella, R. Barbella, J.-N. Rouzaud, A. Tregrossi, A. Ciajolo, Structure–property relationship in nanostructures of young and mature soot in premixed flames, P. Combust. Inst. 32 (2009) 697–704.